Mechanisms of deformation-induced trace element migration in zircon resolved by atom probe and correlative microscopy

Steven M. Reddy[a,b *], Arie van Riessen [a,c], David W. Saxey [a,c], Tim E. Johnson[b], William D. A. Rickard[a,c], Denis Fougerouse[a,b], Sebastian Fischer[d], Ty J. Prosa[e], Katherine P. Rice[e], David A Reinhard[e], Yimeng Chen[e], David Olson[e]

[a] *Geoscience Atom Probe, Advanced Resource Characterisation Facility, John de Laeter Centre, Curtin University, GPO Box U1987, Perth, WA 6845, Australia*

[b] *Department of Applied Geology, The Institute for Geoscience Research (TIGeR), Western Australian School of Mines, Curtin University, GPO Box U1987, Perth, WA 6845, Australia.*

[c] *Department of Physics and Astronomy, Curtin University, GPO Box U1987, Perth, WA 6845, Australia.*

[d] *Department of Earth and Environmental Sciences, University of St Andrews, St Andrews, Fife, KY16 9AL, UK.*

[e] *CAMECA Instruments Inc., 5500 Nobel Drive, Madison, WI 53711, USA.*

* Corresponding author: s.reddy@curtin.edu.au

Keywords:

atom probe microscopy, nanoscale, zircon, trace element, geochemistry, microstructure, EBSD, reidite, impact

Abstract

The widespread use of zircon in geochemical and geochronological studies of crustal rocks is underpinned by an understanding of the processes that may modify its composition. Deformation during tectonic and impact related strain is known to modify zircon trace element compositions, but the mechanisms by which this occurs remain unresolved. Here we combine electron backscatter diffraction, transmission Kikuchi diffraction and atom probe microscopy to investigate trace element migration associated with a ~20 nm wide, 2° low-angle subgrain boundary formed in zircon during a single, high-strain rate, deformation associated with a bolide impact. The low-angle boundary shows elevated concentrations of both substitutional (Y) and interstitial (Al, Mg & Be) ions. The observed compositional variations reflect a dynamic process associated with the recovery of shock-induced vacancies and dislocations into lower energy low-angle boundaries. Y segregation is linked to the migration and localization of oxygen vacancies, whilst the interstitial ions migrate in association with dislocations. These data represent the direct nanoscale observation of geologically-instantaneous, trace element migration associated with crystal plasticity of zircon and provide a framework for further understanding mass transfer processes in zircon.

1. Introduction

Zircon ($ZrSiO_4$) is a common accessory mineral that occurs in most crustal rocks. The low diffusivity of most trace elements through the zircon lattice, inferred from trace element zonation (Vavra, 1990; Hoskin, 2000) and diffusion experiments (Cherniak et al., 1997; Cherniak and Watson, 2003; Cherniak and Watson, 2007), make zircon a robust geochemical repository. Hence, the trace and rare earth elements (REE) incorporated into the zircon are commonly used to place valuable constraints on petrogenetic processes (Hoskin and Schaltegger, 2003). For example, the trace element geochemistry of zircon yields source rock type and crystallization conditions of igneous rocks (Belousova et al., 2002; Ferry and Watson, 2007; Hanchar and van Westrenen, 2007; Grimes et al., 2009; Claiborne et al., 2010) and can place constraints on recrystallization mechanisms, hydrothermal alteration and the histories of metamorphic rocks (Hoskin and Black, 2000; Hoskin, 2005; Harley et al., 2007; Marsh and Stockli, 2015). The trace element composition of zircon also has economic importance, for example being used to assess the prospectivity of granites for mineralisation (Ballard et al., 2002; Dilles et al., 2015).

The incorporation of trace amounts of uranium, and its subsequent radioactive decay to lead, enables the U-Pb dating of zircon to place temporal constraints of numerous crustal processes (Harley and Kelly, 2007; Corfu, 2013). When combined with Lu-Hf and oxygen isotopic data, zircon can be used to constrain crustal evolution over a range of timescales (Hawkesworth and Kemp, 2006; Parman, 2015; Payne et al., 2016). In addition, the ability of zircon to withstand weathering, erosion, sedimentary transport and diagenesis, make zircon a common target for sedimentary provenance analysis

(Fedo et al., 2003; Gehrels, 2014) and the geochemistry and geochronology of ancient detrital zircon grains is the principal means of understanding petrogenetic processes and environmental conditions in the earliest stages of Earth history (Maas et al., 1992; Wilde et al., 2001; Hoskin, 2005; Watson and Harrison, 2005; Harrison and Schmitt, 2007; Ushikubo et al., 2008; Harrison, 2009). Complementing the terrestrial studies of Hadean zircon are analyses from lunar and meteoritic zircon samples, which provide fundamental constraints on the early solar system and planetary evolution (Nemchin et al., 2010; Humayun et al., 2013; Iizuka et al., 2015). However, despite the broad application of zircon in geochemical and geochronological studies, it is widely recognised that a number of different processes may modify the trace element compositions of zircon.

Radiation damage within zircon can facilitate trace element redistribution and the incorporation of non-formula elements (Ewing et al., 2003; Palenik et al., 2003; Horie et al., 2006) even under low temperature hydrothermal conditions (Geisler et al., 2002; Pidgeon, 2014). Trace element modification associated with radiation damage reflects a complex interaction of the self-irradiation process, enhanced diffusion along radiation-induced defects, and reactions associated with fluid ingress by radiation-enhanced fractures and recrystallization (Geisler et al., 2007; Nasdala et al., 2010).

Detailed microstructural characterisation has demonstrated that crystal plastic deformation of zircon may take place in Earth's crust due to tectonic processes (Reddy et al., 2007; Reddy et al., 2009; Piazolo et al., 2012) and meteorite impact events (Moser et al., 2011; Cavosie et al., 2015). Geochemical analyses of deformed zircon indicate that trace element compositions may be modified in the vicinity of intracrystalline defects,

92 particularly in the regions of low-angle boundaries (Reddy et al., 2006; Timms et al.,
93 2006; Moser et al., 2009; Nemchin et al., 2009; Moser et al., 2011; Timms et al., 2011;
94 Piazolo et al., 2016). A number of models have been proposed to explain the observed
95 relationship between microstructure and trace element migration including enhanced
96 diffusion along dislocation pipes and low-angle boundaries (Reddy et al., 2006; Moser et
97 al., 2011; Timms et al., 2011; Piazolo et al., 2016), incorporation of trace elements within
98 migrating dislocations (Reddy et al., 2006; Reddy et al., 2007; Piazolo et al., 2016) and
99 creep cavitation (Timms et al., 2012a). However, crystal defects may also trap trace
100 elements; for example, Pb has been shown to segregate into dislocation loops during
101 metamorphism (Peterman et al 2016).
102
103 Constraining the processes that are responsible for deformation-related compositional
104 modification of zircon has remained elusive because the volume of material typically
105 needed to characterise compositional heterogeneities (100s of μm^3) is considerably
106 larger than the sub-micron scale microstructures in which these heterogeneities occur.
107 Direct comparison with compositional data has required averaging of quantitative
108 microstructural data over similar volumes to those measured by quantitative analytical
109 techniques (Timms et al., 2006; Timms et al., 2011). Higher spatial resolution analytical
110 methods, for example, hyperspectral cathodoluminescence (CL) data, indicate variations
111 in the concentrations of trivalent REEs at the micrometre scale, but these are not
112 quantitative (Reddy et al., 2006; Timms and Reddy, 2009; Timms et al., 2011). As a
113 result, the spatial relationships between deformation microstructures and
114 compositional variations, as well as the processes responsible for trace element mobility
115 in deformed or defect-enriched zircon, have proved difficult to resolve.
116

The recent applications of atom probe microscopy to zircon have highlighted the potential for this analytical technique to quantify nanoscale compositional variations and establish the controls and processes associated with trace element modification (Valley et al., 2014; Valley et al., 2015; Peterman et al., 2016; Piazolo et al., 2016). Here we combine electron backscatter diffraction (EBSD), transmission Kikuchi diffraction (TKD) and atom probe microscopy to investigate the nanoscale relationships between microstructure and trace element composition in a zircon grain that records a single, shock deformation event associated with a meteorite impact.

2. Sample and Analytical Procedures

2.1 Sample Description

The Stac Fada Member of the Stoer Group of sedimentary rocks in NW Scotland represents an ejecta deposit associated with a meteorite impact ~1.18 billion years ago (Amor et al., 2008; Parnell et al., 2011; Reddy et al., 2015). The unit extends some 50 km along strike and has a variable thickness that in places exceeds 20 m (Fig. 1). It comprises three main facies types attributed to deposition from a single decelerating granular density current (Branney and Brown, 2011). The analysed sample (14-SF-01) was collected from the basal layer of the Stac Fada Member (UK Grid Reference NC 03348 28515 equivalent to Latitude 58.2014, Longitude -5.3482 in WGS84) (Fig. 1) and is a matrix-supported, poorly-sorted breccia comprising centimetre size clasts of lithic and devitrified melt fragments. The sample shows no evidence of deformation or metamorphism at the hand specimen scale. This is consistent with previous reports that the Stac Fada Member underwent diagenesis immediately after deposition (Parnell et al., 2011) and has only undergone low-grade (prehnite-pumpellyite facies) regional metamorphism and negligible post-impact deformation (Simms, 2015).

143

144 *2.2 Methodologies*

145

146 Details of the zircon separation, concentration and mounting methodologies have been

147 described in detail elsewhere (Reddy et al., 2015) and only a brief summary is provided

148 here.

149

150 Approximately 2 kg of sample 14-SF-01 was disaggregated using SelFrag high-voltage

151 pulse power fragmentation at the Department of Applied Geology, Curtin University.

152 Short pulses of high-voltage electrical fields were applied with a frequency of 2 Hz over

153 a decreasing range of voltages and electrode gaps. As the sample was progressively

154 disaggregated, grains and fragments smaller than 410 μm fell through an integrated

155 mesh and into a collection vessel, which is isolated from further electrical pulses.

156 Previous studies indicate that SelFrag does not lead to significant increases in the

157 temperature or pressure of the separated phases and has no noticeable effect on zircon

158 grains (Giese et al., 2010).

159

160 The disaggregated sample was sieved using a 355 μm disposable mesh and sodium

161 polytungstate (NaPT) solution (specific gravity =2.85) was used to concentrate zircon

162 grains in the <355 μm fraction. A hand magnet was used to remove the magnetic

163 fraction and the remaining grains were passed through a Franz magnetic separator with

164 the magnetic fractions being drawn off in increments of 0.2 to 0.5 amps over a range of

165 current settings from 0.1 to 1.7A. The non-magnetic (>1.7A) fraction was then hand-

166 picked for zircon. Approximately 200 separated zircon grains were investigated but data

167 from only one of these (grain 86) are reported here.

168

169 EBSD and CL imaging of grain 86 was conducted on a Tescan MIRA3 Field Emission SEM
170 with Oxford Instruments AZtec EBSD system, housed in the Microscopy & Microanalysis
171 Facility (John de Laeter Centre) at Curtin University. CL imaging was undertaken using a
172 Tescan panchromatic CL detector with 185-850 nm spectral range at 10 kV accelerating
173 voltage and a working distance of 16mm. EBSD data were acquired using the automatic
174 mapping capability of Oxford Instruments AZtec 2.3 software. Match units used for
175 indexing were derived from published crystallographic data for zircon (Hazen and
176 Finger, 1979) and reidite (Farnan et al., 2003). For grain 86, a 200 nm grid was used to
177 systematically collect ~530,000 electron backscatter patterns. The EBSD data were
178 post-processed using Oxford Instruments Channel 5.12 software to remove 'wildspikes'
179 and interpolate non-indexed points using a 6 or 7 nearest neighbour filter following
180 standard procedures for zircon EBSD analysis (Reddy et al., 2007). The post-processed
181 data files were then used to generate EBSD maps.
182
183 Atom probe microscopy is a technique that allows the sub-nanometre scale, 3D imaging
184 of atoms across the whole periodic table (Kelly and Larson, 2012; Larson et al., 2013b).
185 The technique involves time-controlled field evaporation of atoms by applying a high-
186 voltage electric field to a needle-shaped sample whose tip is then heated by a pulsing UV
187 laser. Ideally, the instrument is set up such that a single atom is field evaporated every
188 ~100 laser pulses. On evaporation, the atom is immediately ionised and accelerated by
189 the field toward a position-sensitive detector. The x–y coordinates of the detector
190 impact, combined with the order in which the ions hit the detector, allows
191 reconstruction of the original position of the atoms in the sample (Gault et al., 2009;
192 Larson et al., 2013a). The time-of-flight between the laser pulse and the detector impact
193 is a function of the mass-to-charge ratio (m/z) of the emitted ion, and is used to identify

194 the atom species emitted from the tip. The charge of the emitted ion does not represent
195 the original charge of the species in the analysed sample, but is induced by the electric
196 field immediately after evaporation (Kingham, 1982). This charge is therefore largely a
197 function of experimental run conditions and specimen morphology (Larson et al.,
198 2013b).
199
200 The mass spectrometry data is reported in the form of a histogram (mass spectrum), in
201 which the number of counts is plotted against intervals in m/z. Peaks in the mass
202 spectrum that sit above the background noise level are identified and delineated
203 manually; a process referred to as 'ranging'. The ions that form the ranged peaks are
204 then used, with their x, y and z positions, to reconstruct the chemical identities and
205 original 3D locations of the analysed atoms. Typical data sets comprise millions to tens
206 of millions of atoms.
207
208 In contrast to most zircon analytical approaches, atom probe microscopy does not use a
209 standard in the same manner as in ion- and electron-probe techniques. Ionisation yield
210 and detection efficientcy are constant for all elements (Kingham, 1982; Straub et al.,
211 1999). Furthermore, the APM technique does not lend itself to correction using
212 standards as the analysis conditions cannot be reliably replicated between the standard
213 and the specimen of interest. In general, the voltage applied to the specimen, the heating
214 from the laser pulse and the shape of the specimen tip cannot be held constant between
215 two acquisitions, and it is not clear that a discrepancy in the result from the standard
216 analysis can be carried over and applied directly to the data of interest. However, past
217 experience with other materials, and more recent APM studies of zircon (Valley et al.,

2014; Valley et al., 2015; Peterman et al., 2016; Piazolo et al., 2016) provide a basis for confidence in the measured concentrations of trace elements reported here.

Atom probe specimens were prepared by focussed ion beam milling at CAMECA Instruments Inc., Madison, Wisconsin, USA. A region of interest, identified from the EBSD data, was targeted for site-specific atom probe sample preparation. A FEI Helios Nanolab 660 dual beam FIB-SEM was used to fabricate atom probe specimens on a microtip coupon (Thompson et al., 2007b). Tip sharpening was undertaken using several annular milling steps, each with progressively smaller inner radii and reduced beam currents. A final cleaning at 5kV was undertaken to remove most of the ion-milling induced gallium and surface contamination.

During the sharpening process, TKD analysis of the atom probe needle was carried out on a FEI Nova NanoLab 600 dual beam FIB-SEM equipped with an EBSD system from EDAX. TKD is capable of providing high spatial resolution orientation mapping for atom probe specimens (Babinsky et al., 2014) and was conducted with a 20 kV electron beam with a step size of ~10 nm. TKD data acquired using the EDAX system were exported as .ang files and post-processed using Oxford Instruments Channel 5.12 software.

Atom probe results were acquired using the CAMECA LEAP 5000 XR in laser pulsing mode with initial and final voltages of 3.2 kV and 4.6 kV respectively. Data acquisition utilised a 355 nm laser with pulse energy of ~250 pJ, focussed to a spot-size less than 0.5 μm at the specimen apex, and operating at a frequency ~180 kHz. The specimens were kept at a temperature of 30 K to inhibit thermally induced ion migration on the tip

242 surface during field ionisation, and the ion detection rate was set to 0.01 ions per pulse
243 (Larson et al., 2013b).
244
245 Atom probe data were acquired using LAS Root version 15.41.351, reconstructed with
246 CAMECAROOT version 15.43.393e, and analysed with version 3.6.10 of Cameca's
247 Interactive Visualisation and Analysis Software (IVAS). m/z values from 0 to 300 Da
248 were recorded, and the background throughout the experiment was around 20
249 ppm/nsec, as reported by CAMECAROOT. The mass resolving power for the time-of-
250 flight spectrum ($M/\Delta M$) was measured at ~1150 for the $^{16}O_2^+$ peak. For peak ranging,
251 mass peaks were compared to the local background and only those regions above twice
252 the background level were ranged. The reconstruction stage used an initial tip radius of
253 25nm, and a constant shank angle of 5°. Features observed by SE imaging and TKD were
254 adopted to validate the parameters used in 3D reconstruction.
255
256 Trace element chemical analysis was performed using a combination of iso-
257 concentration surfaces (iso-surfaces) and proximity histograms (proxigrams). An iso-
258 surface is a 2-dimensional contour of constant chemical concentration, with regions
259 above a threshold level of concentration on one side of the boundary and lower
260 concentrations on the other. Proxigrams are 1-dimensional concentration profiles that
261 are plotted against the perpendicular distance from a particular iso-surface. Iso-surfaces
262 are generally curved, and the proxigram analysis conducted by IVAS uses a sophisticated
263 algorithm to calculate distances from the reference surface (Hellman et al., 2000).
264
265 **3. Results**

Cathodoluminescence imaging of grain 86 shows a complicated microstructure comprising a dark CL-poor core surrounded by intermediate region and a bright CL rim (Fig. 2a). A band contrast map of the zircon grain, which reflects the quality of EBSD patterns in different parts of the grain, shows additional complexity in the dark CL core. A series of ~2 μm wide, parallel lamellae, seen in both CL and band contrast maps, cut across the brighter CL zones, but do not penetrate into the dark CL core. These bands are shown by the EBSD data to be reidite, the high-pressure $ZrSiO_4$ polymorph (Fig. 2c). This reidite, the focus of a previous study (Reddy et al., 2015), along with the host zircon, record variations in lattice orientation expressed by the presence of discrete low-angle orientation boundaries that each accommodate 0.5–2° of misorientation and together accommodate a total of ~16° lattice variation across the whole grain (Fig. 2c). The distribution of low-angle boundaries in the zircon is complicated but broadly follows the spatial distribution of the reidite (Fig. 2c,d). One of these low-angle boundaries is captured in the atom probe specimen (Fig. 3). This boundary coincides with a ~2° change in orientation recorded by the TKD data (blue-green contact in Fig. 3). In addition, the TKD data indicate that the atom probe specimen comprises only zircon, with no evidence for reidite along the identified orientation boundary (Fig. 3).

Atom probe analysis of the zircon specimen shows a complex mass spectrum, which reflects the evaporation of single ions and molecular species at the +1 to +4 charge states (Fig. 4). Most peaks represent the major elements found in zircon with only a few trace element peaks being detected. The chemical sensitivity of the atom probe is often around 10 ppma, but the exact detection limit depends on the location and number of the expected peaks. Many of the REEs are likely to appear in the mass spectrum as

doubly or triply charged ions, as well as possibly doubly and triply charged oxides. This means that REE peaks may be divided between a large number of mass peaks within the spectrum, significantly diluting the signal strength at any specific m/z value. Minimising this dilution effect, by optimising atom probe acquisition parameters for specific trace elements, is an area of future research.

Reconstruction of the data reveals a ~20 nm wide zone of trace element enrichment associated with the orientation boundary (Fig. 5). The zone shows increased concentrations in Y (0.735 at.%), Al (0.543 at.%), Be (0.055 at.%) and Mg (0.029 at.%) associated with a decrease in Zr (Table 1). These trace element concentrations represent significant increases from those measured in the host zircon (Fig. 5). Proximity histograms for the upper and lower boundaries of the enriched zone show that trace element concentrations are not constant across the low-angle boundary, with Y showing narrow maxima ~3 nm just inside both of the two boundary interfaces, and Al, Be and Mg exhibiting broader maxima around 4–5 nm inside the interfaces (Fig. 6). The concentration of Mg also shows a slight maximum outside the lower interface; a feature that is missing from the upper interface (Fig 5, 6).

Rare earth element, actinide and Pb distributions within the sample are below the detection sensitivity (50-100 ppma, 50 ppma, and 50 ppma respectively) - as determined by the background noise local to these positions within the mass spectrum (Figure 4). Similarly, there is no observable phosphorus peak (~100 ppma detection sensitivity) in the atom probe mass spectrum. This absence of P limits the extent of xenotime (YPO_4) substitution in the zircon lattice. The detection limits are relatively high due to the tails on the mass peaks between 14 and ~100 Da. These elevate the local

315 background noise by up to 10 times its intrinsic value, and make the detection of trace
316 elements in this part of the spectrum more difficult. Several factors may influence the
317 shape of the mass peaks and their tails (Larson et al., 2013b), but the most likely cause
318 in this case is poor thermal conductivity in the atom probe specimen, leading to an
319 extended period of ion evaporation whilst the tip is cooling after the laser pulse.
320
321 **4. Discussion**

322 **4.1 Zircon Microstructure**
323
324 Cathodoluminescence data from a zircon grain from the Stac Fada impactite shows the
325 presence of three CL-distinct zones (Fig. 2a); a dark CL core, a bright CL rim and an
326 intermediate zone between them. Such CL variations in zircon are normally attributed to
327 compositional zoning of trace elements associated with growth (Corfu et al., 2003). In
328 this case, the zones identified in CL are interpreted to represent a complex igneous and
329 metamorphic evolution prior to the reidite-forming impact event. Based on provenance
330 analysis of the Stac Fada zircon population (Rainbird et al., 2001), this evolution is
331 interpreted to reflect the complex tectonic and metamorphic history of the Lewisian
332 target rocks.
333
334 Reidite is the high pressure polymorph of $ZrSiO_4$ (Glass et al., 2002) and its presence in
335 the rims of grain 86 demonstrates that the zircon underwent shock deformation of >30
336 GPa associated with an impact event at ~1.18 Ga (Reddy et al., 2015). Reidite in the
337 grain is limited to the outermost two compositional zones and stops abruptly at the CL
338 dark core. The low CL emission from the core is consistent with radiation-damage
339 associated with the presence of U and Th. Hence, the absence of reidite from the core of
340 the zircon indicates that the formation of reidite is intimately linked to the crystallinity

of the host zircon and that partial metamictization is likely to inhibit the development of reidite in shock environments. This is consistent with previous observations (Wittmann et al., 2006). Furthermore, the observation that low-angle boundaries are preferentially located within the areas of reidite development may indicate that radiation damage of zircon inhibits the formation and/or migration of dislocations.

A bolide impact event would produce an immense number of defects (vacancies and dislocations) within the shocked grain. However, the microstructure of both zircon and reidite is characterised by the presence of discrete low–angle boundaries that each accommodate <2° lattice distortion (Fig. 2c,d). The presence of low-angle boundaries in deformed zircon has previously been interpreted to represent the migration of dislocations into lower energy configurations. Such an interpretation is based on the geometry of the boundary with respect to the crystal lattice (Reddy et al., 2007). The low-angle boundary captured within the atom probe sample, and imaged by TKD analysis, shows no evidence of reidite and accommodates ~2° of misorientation. However, analysis of orientation differences and the low-angle boundary geometry (not presented) are not associated with any previously reported rational zircon slip system (summarised by Timms et al., 2012b). Previous estimates of the dislocation density of 10^{14} m^{-2} in 2° low-angle boundaries associated with tectonic-induced <001>{100} slip (Reddy et al., 2007) are similar to those derived from studies of unrecovered, reidite-bearing, experimentally shock-deformed zircon (Leroux et al., 1999). Thus, we interpret the low-angle boundary in the atom probe specimen to have formed by the migration and complex interaction of a large number of multiple defect types (vacancies and dislocations) that formed almost instantaneously by shock-deformation of zircon.

366 The recovery of minerals by the migration of defects into boundaries may take place in
367 thermal or deformation events that significantly postdate the deformation event that
368 caused them. However, the absence of any significant thermal or deformation events
369 following the deposition of the Stac Fada Member precludes this. The observation that
370 the formation of the low-angle boundaries post-dates the formation of reidite (Reddy et
371 al., 2015), places further temporal constraints on recovery, and indicates that the
372 observed recovery must be related to the latter stages of the impact process. This is
373 consistent with predictions of the evolution of impact-related zircon microstructure
374 based on shock deformation mechanism maps for $ZrSiO_4$ (Timms et al., 2012b). Thus,
375 low-angle boundaries within the zircon are interpreted to reflect immediate post-impact
376 recovery of defects formed during bolide impact.
377
378 **4.2. Trace Element Compositions in the Zircon Host**
379 In undeformed zircon the substitution of trivalent REEs and Y^{3+} for Zr^{4+} requires
380 additional trace element substitutions to maintain charge balance and several different
381 mechanisms have been postulated (Cherniak, 2010). In this study, P is below
382 background noise levels, the ratio of Y to P is therefore high, and there is a spatial
383 correlation between Y and the interstitial elements Al, Mg and Be both in the host zircon
384 and the low-angle boundary. These three interstitial elements are not commonly
385 analysed in zircon. However, when such analyses are undertaken then these elements
386 have been reported to be incorporated into zircon at trace levels during growth (Speer,
387 1980; Hinton and Upton, 1991; Hoskin et al., 2000; Wiedenbeck et al., 2004). Charge
388 compensation substitutions based on the ratio of (REE, Y) to P indicate that the
389 important substitutions within the pre-shocked zircon were probably $(Mg, Be)^{2+}_{(int)} +$
390 $3Y^{3+} + P^{5+} = 3Zr^{4+} + Si$ and $Al^{3+}_{(int)} + 4Y^{3+} + P^{5+} = 4Zr^{4+} + Si$ (Hoskin et al., 2000). Since P in

391 zircon tends to increase with magmatic differentiation, the high, pre-shock, Y/P ratio
392 (>3) of the zircon points to derivation from a mafic source (Hoskin et al., 2000). The
393 presence of hydrated mafic and ultramafic rocks in the impact target zone (Johnson et
394 al., 2012) may explain the presence of spherules of basaltic composition within the Stac
395 Fada Member, a feature that some find difficult to reconcile with a non-volcanic origin
396 for the unit (Goodenough and Krabbendam, 2011).
397
398 **4.3 Trace Element Variations and Microstructure**
399 A model to explain the variations in Y, Al, Mg and Be within the atom probe specimen
400 must account for the spatial coincidence of trace element enrichment and low-angle
401 boundary formation (Figs. 3, 5), and the similar behaviour of both substitutional Y and
402 interstitial Al, Mg and Be ions. The close spatial and temporal relationship between
403 trace element segregation and the low-angle boundary indicates that the two features
404 developed concurrently and are intimately linked. Such an interpretation is consistent
405 with the general observation that increasing lattice misorientations, and therefore
406 increasing dislocation density, are associated with increasing trace element segregation
407 in metals and alloys (Watanabe, 1985).
408
409 The short-range segregation of solute atoms at interfaces is well established in the
410 materials science literature and is recognised as a complex process that is controlled by
411 a range of extrinsic (pressure, temperature) and intrinsic (elastic and electrostatic
412 interactions between solute and host atoms) variables (Sutton and Balluffi, 2006).
413 Although there is very little detailed analysis of such processes in minerals, it is clear
414 that the segregation of trace elements into the low-angle boundary must be
415 energetically favourable compared to maintaining the trace elements in the host zircon.

However, the mechanisms responsible for segregation remain enigmatic and a number of factors may contribute to the driving force for trace element migration.

Principal amongst the drivers for substitutional ion migration is elastic strain energy associated with differences in ionic sizes between the trace element and host. Molecular dynamic and *ab-initio* modelling of point defect formation in zircon indicate that the production and migration of oxygen vacancies is likely to be energetically favourable over other defect sites (Meis and Gale, 1998; Crocombette and Ghaleb, 2001; Park et al., 2001) and the exchange of Y^{3+} on the Zr^{4+} site is likely to be intimately linked to oxygen vacancies for charge compensation (Akhtar and Waseem, 2001). The close relationship between oxygen vacancies and trace element migration may provide an explanation for the observed Y increase within the zircon low-angle boundary with initial segregation of Y due to elastic interactions being charge balanced by subsequent vacancy migration (Sun et al., 2015). However, although such a model explains the observed Y enrichment in the low-angle boundary, it fails to account for the heterogeneous distribution of Y close to the interfaces of the low-angle boundary (Fig. 6).

Hybrid Monte Carlo – molecular dynamic simulations of Y-stabilised zirconia (ZrO_2) predict the migration of oxygen vacancies into lattice orientation boundaries, due to lower vacancy energies at these microstructural locations, rather than being driven by elastic strain associated with ion size differences (Lee et al., 2013). In ZrO_2, it is energetically favourable for these oxygen vacancies to be associated with yttrium ions (Yoshiya and Oyama, 2011; Lee et al., 2013) and segregation reduces lattice strains in the boundary (Yoshiya and Oyama, 2011). Although such models cannot be quantitatively applied to $ZrSiO_4$, the qualitative distribution of Y^{3+} for Zr^{4+} associated

441 with lattice orientation boundaries in ZrO_2 (Lee et al., 2013) are similar to the peaks of Y
442 distribution recorded by the atom probe data for $ZrSiO_4$ in this study (Fig. 6). Based on
443 the atom probe data presented here, this model seems to be a more likely mechanism
444 than diffusion of Y driven solely by elastic strain.
445
446 In addition to substitutional Y ions, the low-angle boundary is also enriched in the
447 interstitial trace elements Al, Mg and Be. The relationship between interstitial trace
448 elements and dislocations is well known. Modelling of the elastic field around a
449 dislocation predicts that interstitial atoms will concentrate around stationary
450 dislocations (Cottrell and Bilby, 1949); a feature referred to as a "Cottrell atmosphere".
451 Migrating dislocations may capture interstitial elements and continue to move.
452 However, increasing concentrations of interstitial elements around an individual
453 dislocation may halt its migration. Hence, the interstitial nature of Al, Mg and Be ions in
454 the low-angle boundary is consistent with a two-stage process of interstitial migration
455 into Cottrell atmospheres around shock-induced dislocations and the subsequent
456 migration of both the dislocations and interstitial Cottrell atmospheres into low-angle
457 boundaries during post-impact recovery. The additional complication of the asymmetric
458 distribution of Mg immediately outside the lower interface of our sample may reflect
459 asymmetric energy distributions outside the dislocation plane as modelled by kinetic
460 Monte Carlo simulations of dislocation planes in silicon (Portavoce and Tréglia, 2014).
461
462 In contrast to non-geological materials where Cottrell atmospheres have been imaged
463 (Blavette et al., 1999; Thompson et al., 2007a), there has been very little evidence for
464 formation of Cottrell atmospheres in deforming minerals. Ando et al (2001) suggested a
465 Cottrell atmosphere model for Fe–Mg variations associated with low-angle boundaries

466 in olivine. A similar model has been inferred to explain Y mobility in tectonically
467 deformed zircon (Piazolo et al., 2016). However, since Fe–Mg and Y–Zr exchange in
468 these minerals is substitutional in nature, these observations cannot be explained by a
469 Cottrell atmosphere model. A similar point has been made (Portavoce and Tréglia, 2014)
470 regarding interpretations of Cottrell atmospheres from atom probe studies of
471 semiconductors (Thompson et al., 2007a; Duguay et al., 2010). In contrast, the data
472 presented here provides compelling evidence for formation of Cottrell atmospheres
473 associated with interstitial trace elements in zircon.
474
475 **4.4 A model for trace element mobility in shocked zircon**
476 We interpret the enrichment of trace elements in the low-angle boundary to represent a
477 combination of (a) the migration of shock-induced oxygen vacancies into low-energy
478 configurations at the low-angle boundary interface, coupled with segregation of Y into
479 low energy sites, and (b) interstitial migration of Al, Mg and Be as Cottrell atmospheres
480 associated with dislocations that are migrating into low-angle boundary walls. The
481 result is a charge compensated region of lattice distortion comprising both the enhanced
482 substitutional and interstitial trace elements, as measured by the atom probe.
483
484 The nanoscale data presented here provide constraints on the processes by which trace
485 element migration may occur in shock-deformed zircon. The data point to the important
486 role of defect mobility, both vacancies and dislocations, in controlling the respective
487 migration of both substitutional and interstitial ions. The high-strain rate nature of the
488 impact, plus the extremely limited time for subsequent thermal modification of the
489 zircon microstructure, indicate that the measured element migration is an extremely

rapid and dynamic process, likely to be operating at the scale of seconds, linked to defect formation and mobility.

Similar relationships between microstructures and trace elements have been reported for tectonically-deformed zircon (Reddy et al., 2006; Timms et al., 2006; Timms and Reddy, 2009; Timms et al., 2011). These examples showed that defect mobility may also be the driver of the compositional modification of zircon during tectonic deformation. The observed relationships between low-angle boundary and trace element enrichment in zircon has often been considered to reflect fast diffusion of ions along the damaged core of a low-angle boundary (Reddy et al., 2006). However, such a long-range model does not explain variations in trace element compositions within the boundary zone and is not consistent with the short timescale available for the impact event. Although, fast diffusion along the low-angle boundary cannot be ruled out (Piazolo et al., 2016), the observations from the Stac Fada zircon are consistent with short-range mechanisms of low-angle boundary enrichment.

5. Conclusions

This research presents detailed quantitative microstructural analysis and compositional information at the nanoscale to yield unique insights into the relationships between deformation and the migration of chemical species in zircon during a single, high strain-rate, impact event. The data show that there is a clear spatial relationship between trace element compositions and low-angle boundaries formed by the recovery of defects in the later stages of the impact process. Migration of substitutional ions (Y) is associated with the migration of impact-induced oxygen vacancies to the lower energy sites associated with low-angle boundaries rather than elastic strain energies in the lattice.

515 Interstitial ions (Al, Mg, Be) are inferred to migrate by the formation and migration of
516 Cottrell atmospheres around impact-induced dislocations. The analysis of nanoscale
517 compositional variations in zircon by atom probe microscopy provides a framework for
518 understanding the processes controlling the migration and modification of trace
519 element compositions in deforming zircon.
520

521 **Acknowledgments**

522 The Advanced Resource Characterisation Facility (ARCF) comprises state-of-the-art
523 equipment to address fundamental science questions related to the resource sector. The
524 facility is being developed under the auspices of the National Resource Sciences Precinct
525 (NRSP) – a collaboration between CSIRO, Curtin University and The University of
526 Western Australia – and is supported by the Science and Industry Endowment Fund
527 (SIEF RI13-01). The authors gratefully acknowledge support of Curtin University's
528 Microscopy & Microanalysis Facility and the John de Laeter Centre, whose
529 instrumentation has been supported by University, State and Commonwealth
530 Government funding. SMR acknowledges support from the ARC Core to Crust Fluid
531 System COE (CE11E0070). We thank two anonymous reviewers and editor, Christian
532 Koeberl, for constructive comments on the manuscript.
533

Figure Captions

Figure 1. Geological map showing the location of the Stac Fada Member and the sample site. Grid coordinates refer to the Ordnance Survey National Grid coordinate system. This figure is modified after Reddy et al. (2015).

Figure 2. Microstructural maps of the analysed zircon grain. (a) & (b) are after Reddy et al. (2015). (a) Panchromatic CL image showing dark CL core surrounded by an intermediate region and a bright CL rim. Planar black features in the CL emitting zircon are reidite lamellae. Less systematic black lines correspond to healed fractures shown in (b). (b) Band contrast (pattern quality) EBSD map. Brighter greyscale indicates higher pattern quality. (c) EBSD texture component map of zircon (in red) overlain on the band contrast map shown in (b). Lattice orientation variations are shown up to 8° from the white cross and total misorientation across the grain is 16°. Yellow lines show the locations of low-angle boundaries (0.6°–2.0°) within the zircon. Tourquoise lamellae represent reidite. The white square shows the location of map (d). (d) Close up of area in c. The white circle corresponds to the position of the analysed atom probe specimen.

Figure 3. a) Orientation map of the studied atom probe needle constructed from transmission Kikuchi diffraction data. The change from blue to green corresponds to a small-angle lattice misorientation accommodated by a 2° low-angle boundary. White box shows the region of interest analysed by the atom probe following further focussed ion beam milling of the sample. Area below the green area, which has not indexed, reflects low pattern quality due to poor electron transmission through the thicker part of the specimen.

559

560 Figure 4. Atom probe mass spectrum obtained from the region of interest shown in Fig.
561 3. The major m/z peaks are identified, including trace elements that were only present
562 at detectable levels within the boundary region.

563

564 Figure 5. Reconstruction of atom probe data showing trace element variations for Y, Al,
565 Be and Mg. The coloured spheres represent the positions of the illustrated elements but
566 are not drawn to scale. Grey points defining the shape of the atom probe data set
567 represent the positions of 10% of measured Zr atoms. The band showing increased
568 concentration of trace elements corresponds to the position of the low-angle boundary
569 in the region of interest in Fig. 3.

570

571 Figure 6. Proximity histograms showing composition variation in Y, Al, Be and Mg (at.%)
572 as a function of distance from the upper and lower boundary interfaces. The upper and
573 lower interfaces are defined by concentration contours at 0.2 at.% Y.

574

575 **Tables**

576 Table 1. Compositional data from host zircon matrix and low-angle boundary region
577 derived from the atom probe data. Concentrations are in at.%.

578

579

580

581 **References**

582 Akhtar, M. and Waseem, S. (2001) Atomistic simulation studies of zircon. *Chem. Phys.*
583 **274**, 109-120.

584 Amor, K., Hesselbo, S.P., Porcelli, D., Thackrey, S. and Parnell, J. (2008) A precambrian
585 proximal ejecta blanket from Scotland. *Geology* **36**, 303-306.

586 Ando, J., Shibata, Y., Okajima, Y., Kanagawa, K., Furusho, M. and Tomioka, N., Striped iron
587 zoning of olivine induced by dislocation creep in deformed peridotites, *Nature*, 414,
588 2001, 893–895.

589 Babinsky, K., De Kloe, R., Clemens, H. and Primig, S. (2014) A novel approach for site-
590 specific atom probe specimen preparation by focused ion beam and transmission
591 electron backscatter diffraction. *Ultramicroscopy* **144**, 9-18.

592 Ballard, J.R., Palin, M.J. and Campbell, I.H. (2002) Relative oxidation states of magmas
593 inferred from Ce(IV)/Ce(III) in zircon: application to porphyry copper deposits of
594 northern Chile. *Contrib. Mineral. Petrol.* **144**, 347-364.

595 Belousova, E.A., Griffin, W.L., O'Reilly, S.Y. and Fisher, N.I. (2002) Igneous zircon: trace
596 element composition as an indicator of source rock type. *Contrib. Mineral. Petrol.* **143**,
597 602-622.

598 Blavette, D., Cadel, E., Fraczkiewicz, A. and Menand, A. (1999) Three-dimensional
599 atomic-scale imaging of impurity segregation to line defects. *Science* **286**, 2317-2319.

600 Branney, M.J. and Brown, R.J. (2011) Impactoclastic density current emplacement of
601 terrestrial meteorite-impact ejecta and the formation of dust pellets and accretionary
602 lapilli: Evidence from stac fada, Scotland. *J. Geol.* **119**, 275-292.

603 Cavosie, A.J., Erickson, T.M., Timms, N.E., Reddy, S.M., Talavera, C., Montalvo, S.D., Pincus,
604 M.R., Gibbon, R.J. and Moser, D. (2015) A terrestrial perspective on using *ex situ* shocked
605 zircons to date lunar impacts. *Geology* **43**, 999-1002.

606 Cherniak, D. (2010) Diffusion in accessory minerals: zircon, titanite, apatite, monazite
607 and xenotime. *Rev. Mineral. Geochem.* **72**, 827-869.

608 Cherniak, D. and Watson, E. (2007) Ti diffusion in zircon. *Chem. Geol.* **242**, 470-483.

609 Cherniak, D.J., Hanchar, J.M. and Watson, E.B. (1997) Rare-earth diffusion in zircon.
610 *Chem. Geol.* **134**, 289-301.

611 Cherniak, D.J. and Watson, E.B. (2003) Diffusion in zircon. *Rev. Mineral. Geochem.* **53**,
612 113-143.

613 Claiborne, L.L., Miller, C.F. and Wooden, J.L. (2010) Trace element composition of
614 igneous zircon: a thermal and compositional record of the accumulation and evolution of
615 a large silicic batholith, Spirit Mountain, Nevada. *Contrib. Mineral. Petrol.* **160**, 511-531.

616 Corfu, F. (2013) A century of U-Pb geochronology: The long quest towards concordance.
617 *GSA Bulletin* **125**, 33-47.

618 Corfu, F., Hanchar, J.M., Hoskin, P.W.O. and Kinny, P. (2003) Atlas of Zircon Textures. *Rev.*
619 *Mineral. Geochem.* **53**, 469-500.

620 Cottrell, A.H. and Bilby, B.A. (1949) Dislocation theory of yielding and strain ageing of
621 iron. *Proc. Phys.l Soc. A* **62**, 49-62.

622 Crocombette, J.-P. and Ghaleb, D. (2001) Molecular dynamics modeling of irradiation
623 damage in pure and uranium-doped zircon. *J. Nucl. Mater.* **295**, 167-178.

624 Dilles, J.H., Kent, A.J.R., Wooden, J.L., Tosdal, R.M., Koleszar, A., Lee, R.G. and Farmer, L.P.
625 (2015) Zircon compositional evidence for sulfur-degassing from ore-forming arc
626 magmas. *Econ. Geol.* **110**, 241-251.

627 Duguay, S., Philippe, T., Cristiano, F. and Blavette, D. (2010) Direct imaging of boron
628 segregation to extended defects in silicon. *App. Phys. Lett.* **97**, 242104.

629 Ewing, R.C., Meldrum, A., Wang, L., Weber, W.J. and Corrales, L.R. (2003) Radiation
630 effects in zircon. *Rev. Mineral. Geochem.* **53**, 387-425.

631 Farnan, I., Balan, E., Pickard, C.J. and Mauri, F. (2003) The effect of radiation damage on
632 local structure in the crystalline fraction of $ZrSiO_4$: Investigating the ^{29}Si NMR response
633 to pressure in zircon and reidite. *Am. Mineral.* **88**, 1663.

634 Fedo, C.M., Sircombe, K.N. and Rainbird, R.H. (2003) Detrital zircon analysis of the
635 sedimentary record. *Rev. Mineral. Geochem.* **53**, 277-303.

636 Ferry, J.M. and Watson, E.B. (2007) New thermodynamic models and revised
637 calibrations for the Ti-in-zircon and Zr-in-rutile thermometers. *Contrib. Mineral. Petrol.*
638 **154**, 429-437.

639 Gault, B., Moody, M.P., de Geuser, F., Tsafnat, G., La Fontaine, A., Stephenson, L.T., Haley,
640 D. and Ringer, S.P. (2009) Advances in the calibration of atom probe tomographic
641 reconstruction. *J. App. Phys.* **105**, 034913.

642 Gehrels, G. (2014) Detrital Zircon U-Pb Geochronology Applied to Tectonics. *Ann. Rev.*
643 *Earth Planet. Sci.* **42**, 127-149.

644 Geisler, T., Pidgeon, R.T., van Bronswijk, W. and Kurtz, R. (2002) Transport of uranium,
645 thorium, and lead in metamict zircon under low-temperature hydrothermal conditions.
646 *Chem. Geol.* **191**, 141-154.

647 Geisler, T., Schaltegger, U. and Tomaschek, F. (2007) Re-equilibration of zircon in
648 aqueous fluids and melts. *Elements* **3**, 43-50.

649 Giese, J., Seward, D., Stuart, F.M., Wüthrich, E., Gnos, E., Kurz, D., Eggenberger, U. and
650 Schreurs, G. (2010) Electrodynamic disaggregation: Does it affect apatite fission-track
651 and (U-Th)/He Analyses? *Geostand. Geoanal. Res.* **34**, 39-48.

652 Glass, B.P., Liu, S. and Leavens, P.B. (2002) Reidite: An impact-produced high-pressure
653 polymorph of zircon found in marine sediments. *Am. Mineral.* **87**, 562-565.

654 Goodenough, K.M. and Krabbendam, M. (2011) A geological excursion guide to the
655 North-west Highlands of Scotland. NMSE Publishing, Edinburgh, UK. pp.228.

656 Grimes, C.B., John, B.E., Cheadle, M.J., Mazdab, F.K., Wooden, J.L., Swapp, S. and Schwartz,
657 J.J. (2009) On the occurrence, trace element geochemistry, and crystallization history of
658 zircon from *in situ* ocean lithosphere. *Contrib. Mineral. Petrol.* **158**, 757-783.

659 Hanchar, J.M. and van Westrenen, W. (2007) Rare earth element behavior in zircon-melt
660 systems. *Elements* **3**, 37-42.

661 Harley, S.L. and Kelly, N.M. (2007) Zircon - tiny but timely. *Elements* **3**, 13-18.

662 Harley, S.L., Kelly, N.M. and Möller, A. (2007) Zircon behaviour and the thermal histories
663 of mountain chains. *Elements* **3**, 25-30.

664 Harrison, T.M. (2009) The Hadean crust: Evidence from >4 Ga zircons. *Ann. Rev. Earth*
665 *Planet. Sci.* **37**, 479-505.

666 Harrison, T.M. and Schmitt, A.K. (2007) High sensitivity mapping of Ti distributions in
667 Hadean zircons. *Earth Planet. Sci. Lett.* **261**, 9-19.

668 Hawkesworth, C.J. and Kemp, A.I.S. (2006) Using hafnium and oxygen isotopes in zircons
669 to unravel the record of crustal evolution. *Chem. Geol.* **226**, 144-162.

670 Hazen, R.M. and Finger, L.W. (1979) Crystal structure and compressibility of zircon at
671 high pressure. *Am. Mineral.* **64**, 196-201.

672 Hellman, O.C., Vandenbroucke, J.A., Rüsing, J., Isheim, D. and Seidman, D.N. (2000)
673 Analysis of three-dimensional atom-probe data by the proximity histogram. *Microsc.*
674 *Micronanal.* **6**, 437-444.

675 Hinton, R. and Upton, B. (1991) The chemistry of zircon: Variations within and between
676 large crystals from syenite and alkali basalt xenoliths. *Geochim. Cosmochim. Acta* **55**,
677 3287-3302.

678 Horie, K., Hidaka, H. and Gauthier-Lafaye, F. (2006) Elemental distribution in zircon:
679 Alteration and radiation-damage effects. *Phys. Chem. Earth.* **31**, 587-592.

680 Hoskin, P.W.O. (2000) Patterns of chaos: Fractal statistics and the oscillatory chemistry
681 of zircon. *Geochim. Cosmochim. Acta* **64**, 1905-1923.

682 Hoskin, P.W.O. (2005) Trace-element composition of hydrothermal zircon and the
683 alteration of Hadean zircon from the Jack Hills, Australia. *Geochim. Cosmochim. Acta* **69**,
684 637-648.

685 Hoskin, P.W.O. and Black, L.P. (2000) Metamorphic zircon formation by solid-state
686 recrystallization of protolith igneous zircon. *J. Metamorph. Geol.* **18**, 423-439.

687 Hoskin, P.W.O., Kinny, P.D., Wyborn, D. and Chappell, B.W. (2000) Identifying accessory
688 mineral saturation during differentiation in granitoid magmas: an integrated approach.
689 *J. Petrol.* **41**, 1365 -1396.

690 Hoskin, P.W.O. and Schaltegger, U. (2003) The composition of zircon and igneous and
691 metamorphic petrogenesis. *Rev. Mineral. Geochem.* **53**, 27-62.

692 Humayun, M., Nemchin, A., Zanda, B., Hewins, R.H., Grange, M., Kennedy, A., Lorand, J.P.,
693 Gopel, C., Fieni, C., Pont, S. and Deldicque, D. (2013) Origin and age of the earliest
694 Martian crust from meteorite NWA 7533. *Nature* **503**, 513-516.

695 Iizuka, T., Yamaguchi, T., Hibiya, Y. and Amelin, Y. (2015) Meteorite zircon constraints on
696 the bulk Lu−Hf isotope composition and early differentiation of the Earth. *Proc. Nat.*
697 *Acad. Sci. U.S.A.* **112**, 5331-5336.

698 Johnson, T., Fischer, S., White, R., Brown, M. and Rollinson, H. (2012) Archaean
699 intracrustal differentiation from partial melting of metagabbro—field and geochemical
700 evidence from the central region of the Lewisian complex, NW Scotland. *J. Petrol.* **53**,
701 2115-2138.

702 Kelly, T.F. and Larson, D.J. (2012) Atom probe tomography 2012. *Ann. Rev. Mater. Res.*
703 **42**, 1-31.

704 Kingham, D.R. (1982) The post-ionization of field evaporated ions: A theoretical
705 explanation of multiple charge states. *Surf. Sci.* **116**, 273-301.

706 Larson, D.J., Gault, B., Geiser, B.P., De Geuser, F. and Vurpillot, F. (2013a) Atom probe
707 tomography spatial reconstruction: Status and directions. *Curr. Opin. Solid State Mater.*
708 *Sci.* **17**, 236-247.

709 Larson, D.J., Prosa, T.J., Ulfig, R.M., Geiser, B.P. and Kelly, T.F. (2013b) Local Electrode
710 Atom Probe: A User's Guide. Springer-Verlag New York. pp. 318.

711 Lee, H.B., Prinz, F.B. and Cai, W. (2013) Atomistic simulations of grain boundary
712 segregation in nanocrystalline yttria-stabilized zirconia and gadolinia-doped ceria solid
713 oxide electrolytes. *Acta Mater.* **61**, 3872-3887.

714 Leroux, H., Reimold, W.U., Koeberl, C., Hornemann, U. and Doukhan, J.C. (1999)
715 Experimental shock deformation in zircon: a transmission electron microscopic study.
716 *Earth Planet. Sci. Lett.* **169**, 291-301.

717 Maas, R., Kinny, P.D., Williams, I.S., Froude, D.O. and Compston, W. (1992) The Earth's
718 oldest known crust: A geochronological and geochemical study of 3900-4200 Ma old
719 detrital zircons from Mt. Narryer and Jack Hills, Western Australia. *Geochim. Cosmochim.*
720 *Acta* **56**, 1281-1300.

721 Marsh, J.H. and Stockli, D.F. (2015) Zircon U–Pb and trace element zoning characteristics
722 in an anatectic granulite domain: Insights from LASS-ICP-MS depth profiling. *Lithos* **239**,
723 170-185.

724 Meis, C. and Gale, J.D. (1998) Computational study of tetravalent uranium and plutonium
725 lattice diffusion in zircon. *Mater. Sci. Eng.* **B57**, 52-61.

726 Moser, D.E., Cupelli, C.L., Barker, I.R., Flowers, R.M., Bowman, J.R., Wooden, J. and Hart,
727 J.R. (2011) New zircon shock phenomena and their use for dating and reconstruction of

large impact structures revealed by electron nanobeam (EBSD, CL, EDS) and isotopic U-Pb and (U-Th)/He analysis of the Vredefort Dome. *Can. J. Earth Sci.* **48**, 117-139.

Moser, D.E., Davis, W.J., Reddy, S.M., Flemming, R.L. and Hart, R.J. (2009) Zircon U–Pb strain chronometry reveals deep impact-triggered flow. *Earth Planet. Sci. Lett.* **277**, 73-79.

Nasdala, L., Hanchar, J.M., Rhede, D., Kennedy, A.K. and Váczi, T. (2010) Retention of uranium in complexly altered zircon: An example from Bancroft, Ontario. *Chem. Geol.* **269**, 290-300.

Nemchin, A., Timms, N., Pidgeon, R., Geisler, T., Reddy, S. and Meyer, C. (2009) Timing of crystallization of the lunar magma ocean constrained by the oldest zircon. *Nat. Geosci.* **2**, 133-136.

Nemchin, A.A., Grange, M.L. and Pidgeon, R.T. (2010) Distribution of rare earth elements in lunar zircon. *Am. Mineral.* **95**, 273-283.

Palenik, C.S., Nasdala, L. and Ewing, R.C. (2003) Radiation damage in zircon. *Am. Mineral.* **88**, 770-781.

Park, B., Weber, W.J. and Corrales, L.R. (2001) Molecular-dynamics simulation study of threshold displacements and defect formation in zircon. *Phys. Rev. B: Condens. Matter* **64**, 174108.

Parman, S.W. (2015) Time-lapse zirconography: Imaging punctuated continental evolution. *Geochemical Perspectives Letters* **1**, 43-52.

748 Parnell, J., Mark, D., Fallick, A.E., Boyce, A. and Thackrey, S. (2011) The age of the
749 Mesoproterozoic Stoer Group sedimentary and impact deposits, NW Scotland. *J. Geol.*
750 *Soc.* **168**, 349-358.

751 Payne, J.L., McInerney, D.J., Barovich, K.M., Kirkland, C.L., Pearson, N.J. and Hand, M.
752 (2016) Strengths and limitations of zircon Lu-Hf and O isotopes in modelling crustal
753 growth. *Lithos* **248–251**, 175-192.

754 Peterman, E.M., Reddy, S.M., Saxey, D.W., Snoeyenbos, D.R., Rickard, W.D.A., Fougerouse,
755 D. and Kylander-Clark, A.R.C. (2016) Nanogeochronology of a discordant zircon
756 measured by atom probe microscopy of Pb-enriched dislocation loops. *Sci. Adv.* **2**,
757 e1601318.

758 Piazolo, S., Austrheim, H. and Whitehouse, M. (2012) Brittle-ductile microfabrics in
759 naturally deformed zircon: Deformation mechanisms and consequences for U-Pb dating.
760 *Am. Mineral.* **97**, 1544-1563.

761 Piazolo, S., La Fontaine, A., Trimby, P., Harley, S., Yang, L., Armstrong, R. and Cairney, J.M.
762 (2016) Deformation-induced trace element redistribution in zircon revealed using atom
763 probe tomography. *Nat. Comms.* **7**, 10490.

764 Pidgeon, R.T. (2014) Zircon radiation damage ages. *Chem. Geol.* **367**, 13-22.

765 Portavoce, A. and Tréglia, G. (2014) Theoretical investigation of Cottrell atmosphere in
766 silicon. *Acta Mater.* **65**, 1-9.

767 Rainbird, R.H., Hamilton, M.A. and Young, G.M. (2001) Detrital zircon geochronology and
768 provenance of the Torridonian, NW Scotland. *J. Geol. Soc.* **158**, 15-27.

769 Reddy, S.M., Johnson, T.E., Fischer, S., Rickard, W.D.A. and Taylor, R.J.M. (2015)
770 Precambrian reidite discovered in shocked zircon from the Stac Fada impactite,
771 Scotland. *Geology* **43**, 899-902.

772 Reddy, S.M., Timms, N.E., Hamilton, P.J. and Smyth, H.R. (2009) Deformation-related
773 microstructures in magmatic zircon and implications for diffusion. *Contrib. Mineral.*
774 *Petrol.* **157**, 231-244.

775 Reddy, S.M., Timms, N.E., Pantleon, W. and Trimby, P. (2007) Quantitative
776 characterization of plastic deformation of zircon and geological implications. *Contrib.*
777 *Mineral. Petrol.* **153**, 625-645.

778 Reddy, S.M., Timms, N.E., Trimby, P., Kinny, P.D., Buchan, C. and Blake, K. (2006) Crystal-
779 plastic deformation of zircon: A defect in the assumption of chemical robustness.
780 *Geology* **34**, 257-260.

781 Simms, M.J. (2015) The Stac Fada impact ejecta deposit and the Lairg Gravity Low:
782 evidence for a buried Precambrian impact crater in Scotland? *Proc. Geol. Assoc.* **126**,
783 742-761.

784 Speer, J.A. (1980) Zircon, in: Ribbe, P.H. (Ed.), *Orthosilicates*. Mineralogical Society of
785 America, Washington D.C., pp. 67-112.

786 Straub, H.C., Mangan, M. A., Lindsay, B.G., Smith, K.A. and Stebbings, R.F., Absolute
787 detection efficiency of a microchannel plate detector for kilo-electron volt energy
788 ions, *Rev. Sci. Instrum.* **70**, 1999, 4238-4240.

789 Sun, L., Marrocchelli, D. and Yildiz, B. (2015) Edge dislocation slows down oxide ion
790 diffusion in doped CeO_2 by segregation of charged defects. *Nat. Comms.* **6**, 6294.

791 Sutton, A. and Balluffi, R. (2006) Interfaces in Crystalline Materials. OUP Oxford, UK. pp.
792 852.

793 Thompson, K., Flaitz, P.L., Ronsheim, P., Larson, D.J. and Kelly, T.F. (2007a) Imaging of
794 arsenic Cottrell atmospheres around silicon defects by three-dimensional atom probe
795 tomography. *Science* **317**, 1370-1374.

796 Thompson, K., Lawrence, D., Larson, D.J., Olson, J.D., Kelly, T.F. and Gorman, B. (2007b) In
797 situ site-specific specimen preparation for atom probe tomography. *Ultramicroscopy*
798 **107**, 131-139.

799 Timms, N.E., Kinny, P.D. and Reddy, S.M. (2006) Enhanced diffusion of Uranium and
800 Thorium linked to crystal plasticity in zircon. *Geochem. Trans.* **7**:10.

801 Timms, N.E., Kinny, P.D., Reddy, S.M., Evans, K., Clark, C. and Healy, D. (2011)
802 Relationship among titanium, rare earth elements, U-Pb ages and deformation
803 microstructures in zircon: Implications for Ti-in-zircon thermometry. *Chem. Geol.* **280**,
804 33-46.

805 Timms, N.E. and Reddy, S.M. (2009) Response of cathodoluminescence to crystal-plastic
806 deformation in zircon. *Chem. Geol.* **261**, 11-23.

807 Timms, N.E., Reddy, S.M., Fitz Gerald, J.D., Green, L. and Muhling, J.R. (2012a) Inclusion-
808 localised crystal-plasticity, dynamic porosity, and fast-diffusion pathway generation in
809 zircon. *J. Struct. Geol.* **35**, 78-89.

810 Timms, N.E., Reddy, S.M., Healy, D., Nemchin, A.A., Grange, M.L., Pidgeon, R.T. and Hart, R.
811 (2012b) Resolution of impact-related microstructures in lunar zircon: A shock-
812 deformation mechanism map. *Meteorit. Planet. Sci.* **47**, 120-141.

Ushikubo, T., Kita, N.T., Cavosie, A.J., Wilde, S.A., Rudnick, R.L. and Valley, J.W. (2008) Lithium in Jack Hills zircons: Evidence for extensive weathering of Earth's earliest crust. *Earth Planet. Sci. Lett.* **272**, 666-676.

Valley, J.W., Cavosie, A.J., Ushikubo, T., Reinhard, D.A., Lawrence, D.F., Larson, D.J., Clifton, P.H., Kelly, T.F., Wilde, S.A. and Moser, D.E. (2014) Hadean age for a post-magma-ocean zircon confirmed by atom-probe tomography. *Nat. Geosci.* **7**, 219-223.

Valley, J.W., Reinhard, D.A., Cavosie, A.J., Ushikubo, T., Lawrence, D.F., Larson, D.J., Kelly, T.F., Snoeyenbos, D. and A, S. (2015) Nano- and Micro-geochronology in Hadean and Archean Zircons by Atom-Probe Tomography and SIMS: New Tools for Old Minerals. *Am. Mineral.* **100**, 1355-1377.

Vavra, G. (1990) On the kinematics of zircon growth and its petrogenetic significance: a cathodoluminescence study. *Contrib. Mineral. Petrol.* **106**, 90-99.

Watanabe, T. (1985) Structural effects on grain boundary segregation, hardening and fracture. *J. Phy. C.* **46**, 555-566.

Watson, E.B. and Harrison, T.M. (2005) Zircon thermometer reveals minimum melting conditions on earliest Earth. *Science* **308**, 841-844.

Wiedenbeck, M., Hanchar, J.M., Peck, W.H., Sylvester, P., Valley, J., Whitehouse, M., Kronz, A., Morishita, Y., Nasdala, L., Fiebig, J., Franchi, I., Girard, J.P., Greenwood, R.C., Hinton, R., Kita, N., Mason, P.R.D., Norman, M., Ogasawara, M., Piccoli, P.M., Rhede, D., Satoh, H., Schulz-Dobrick, B., Skår, O., Spicuzza, M.J., Terada, K., Tindle, A., Togashi, S., Vennemann, T., Xie, Q. and Zheng, Y.F. (2004) Further characterisation of the 91500 zircon crystal. *Geostand. Geoanal. Res.* **28**, 9-39.

Wilde, S.A., Valley, J.W., Peck, W.H. and Graham, C.M. (2001) Evidence from detrital zircons for the existence of continental crust and oceans on the Earth 4.4 Gyr ago. *Nature* **409**, 175-178.

Wittmann, A., Kenkmann, T., Schmitt, R.T. and Stoffler, D. (2006) Shock-metamorphosed zircon in terrestrial impact craters. *Meteorit. Planet. Sci.* **41**, 433-454.

Yoshiya, M. and Oyama, T. (2011) Impurity and vacancy segregation at symmetric tilt grain boundaries in Y_2O_3-doped ZrO_2. *J. Mater. Sci.* **46**, 4176-4190.

Table

	Matrix		Low-angle boundary	
Element	Concentration	+/- (1σ)	Concentration	+/- (1σ)
Zr	17.71%	0.03%	16.03%	0.09%
Si	15.61%	0.03%	15.88%	0.09%
O	66.51%	0.07%	66.54%	0.23%
Hf	0.141%	0.002%	0.106%	0.007%
Y	0.013%	0.001%	0.735%	0.019%
Al	0.0041%	0.0004%	0.543%	0.016%
Be	0.0044%	0.0004%	0.055%	0.005%
Mg	-	-	0.029%	0.004%

Reddy et al (2016). Figure 1

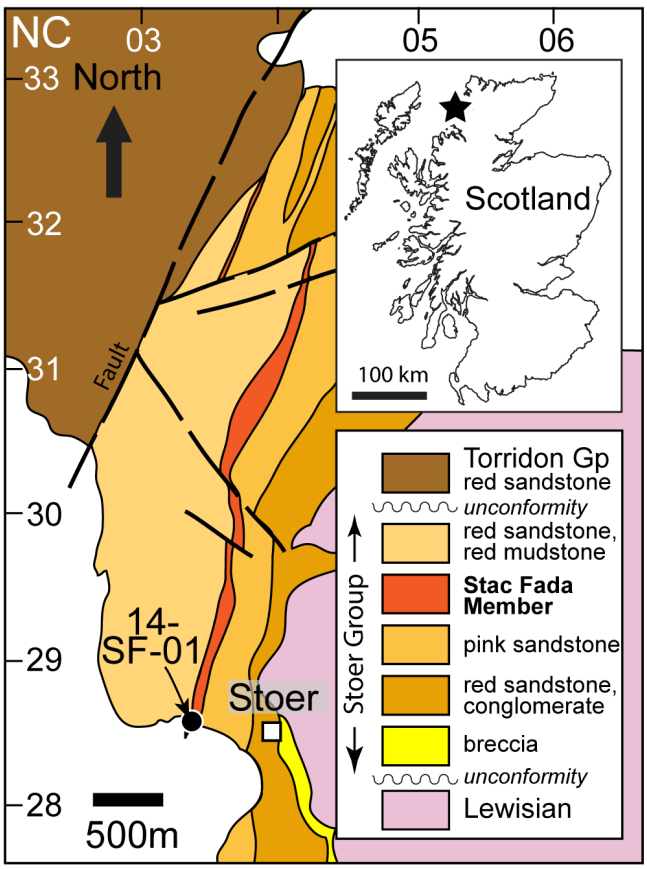

Reddy, S.M., van Riessen, Saxey, D.W., Johnson, T.E., Rickard, W.D.A, Fougerouse, D., Fischer, S., Prosa, T.J., Rice, K.P., Reinhard, D.A., Chen, Y. & Olson, D. 2016. Mechanisms of deformation-induced trace element migration in zircon resolved by atom probe and correlative microscopy. Geochimica et Cosmochimica Acta (2016)

DOI: http://dx.doi.org/10.1016/j.gca.2016.09.019

Reddy et al (2016). Figure 2

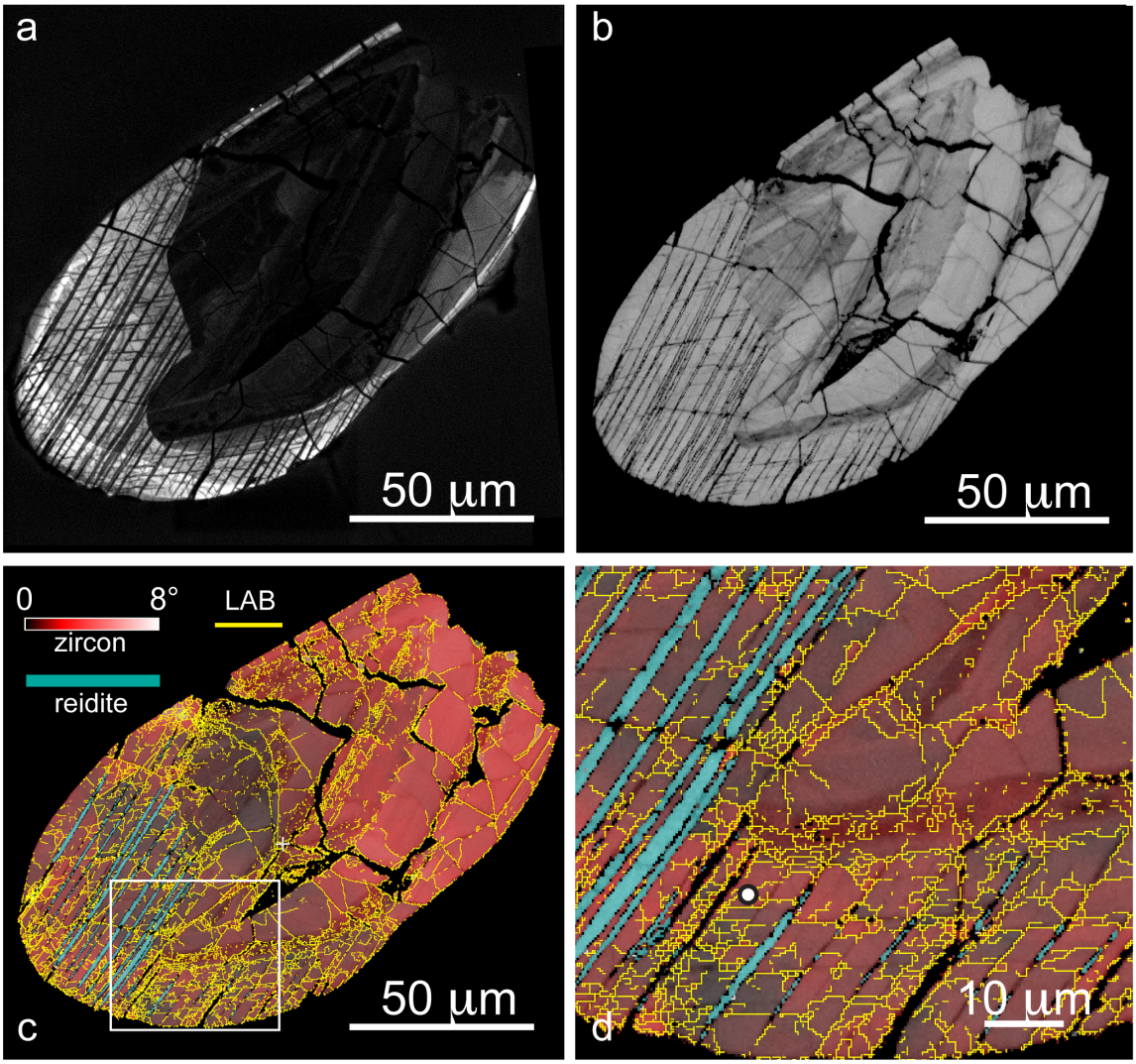

Reddy, S.M., van Riessen, Saxey, D.W., Johnson, T.E., Rickard, W.D.A, Fougerouse, D., Fischer, S., Prosa, T.J., Rice, K.P., Reinhard, D.A., Chen, Y. & Olson, D. 2016. Mechanisms of deformation-induced trace element migration in zircon resolved by atom probe and correlative microscopy. Geochimica et Cosmochimica Acta (2016)

DOI: http://dx.doi.org/10.1016/j.gca.2016.09.019

Reddy et al (2016). Figure 3

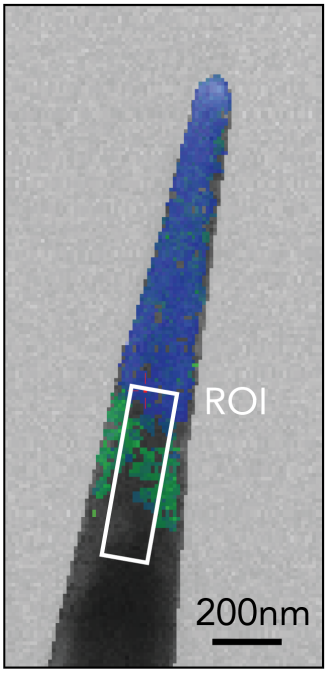

Reddy, S.M., van Riessen, Saxey, D.W., Johnson, T.E., Rickard, W.D.A, Fougerouse, D., Fischer, S., Prosa, T.J., Rice, K.P., Reinhard, D.A., Chen, Y. & Olson, D. 2016. Mechanisms of deformation-induced trace element migration in zircon resolved by atom probe and correlative microscopy. Geochimica et Cosmochimica Acta (2016)

DOI: http://dx.doi.org/10.1016/j.gca.2016.09.019

Reddy et al (2016). Figure 4

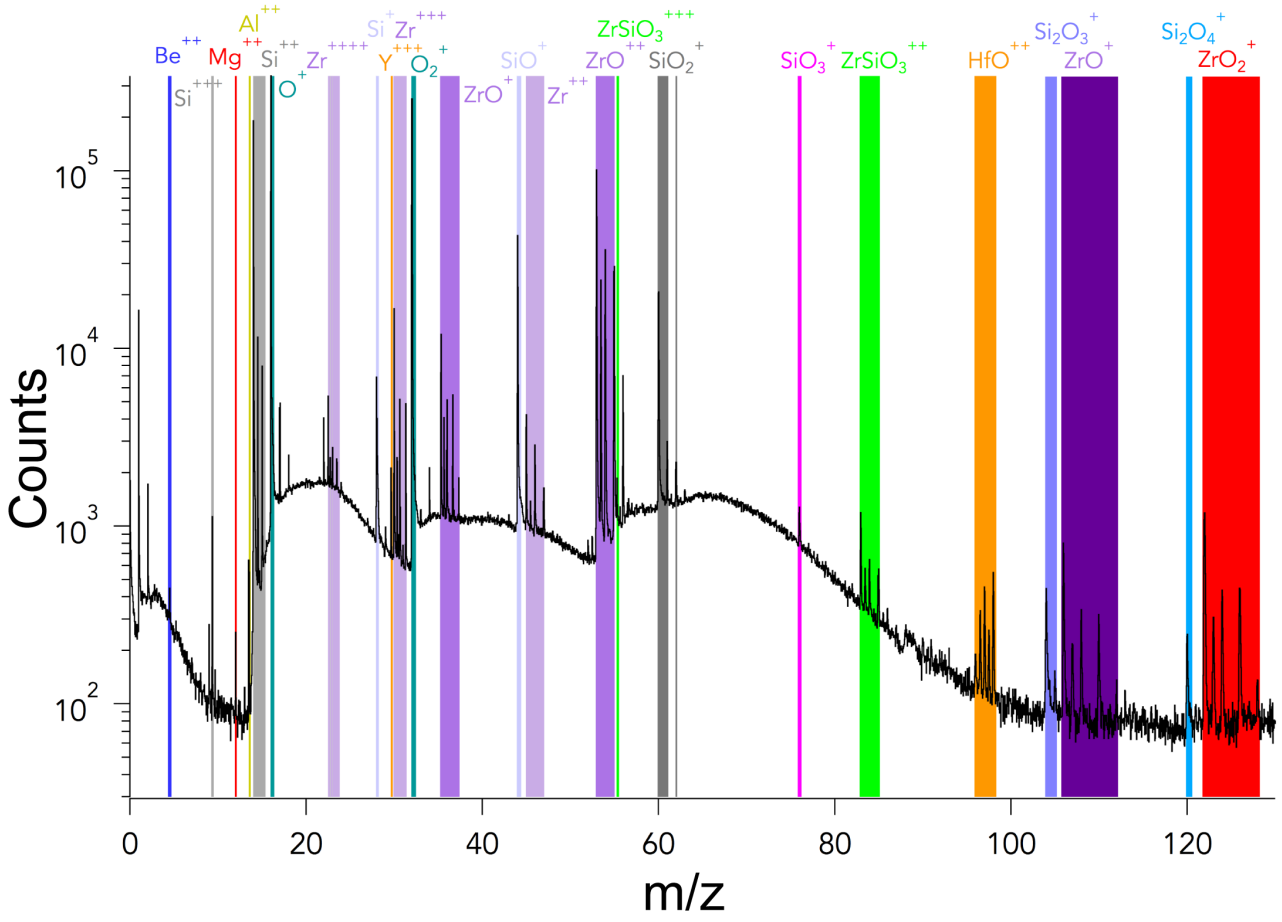

Reddy, S.M., van Riessen, Saxey, D.W., Johnson, T.E., Rickard, W.D.A, Fougerouse, D., Fischer, S., Prosa, T.J., Rice, K.P., Reinhard, D.A., Chen, Y. & Olson, D. 2016. Mechanisms of deformation-induced trace element migration in zircon resolved by atom probe and correlative microscopy. Geochimica et Cosmochimica Acta (2016)

DOI: http://dx.doi.org/10.1016/j.gca.2016.09.019

Reddy et al (2016). Figure 5

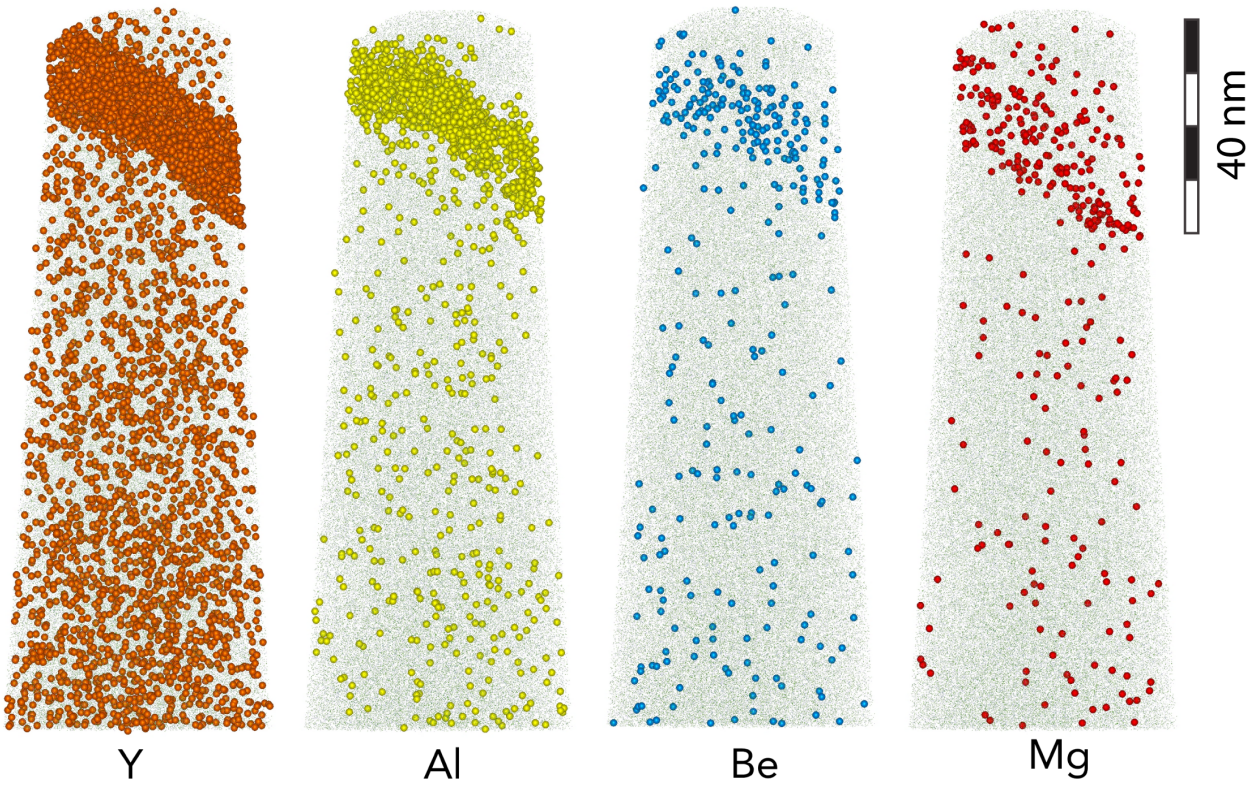

Reddy, S.M., van Riessen, Saxey, D.W., Johnson, T.E., Rickard, W.D.A, Fougerouse, D., Fischer, S., Prosa, T.J., Rice, K.P., Reinhard, D.A., Chen, Y. & Olson, D. 2016. Mechanisms of deformation-induced trace element migration in zircon resolved by atom probe and correlative microscopy. Geochimica et Cosmochimica Acta (2016)

DOI: http://dx.doi.org/10.1016/j.gca.2016.09.019

Reddy et al (2016). Figure 6

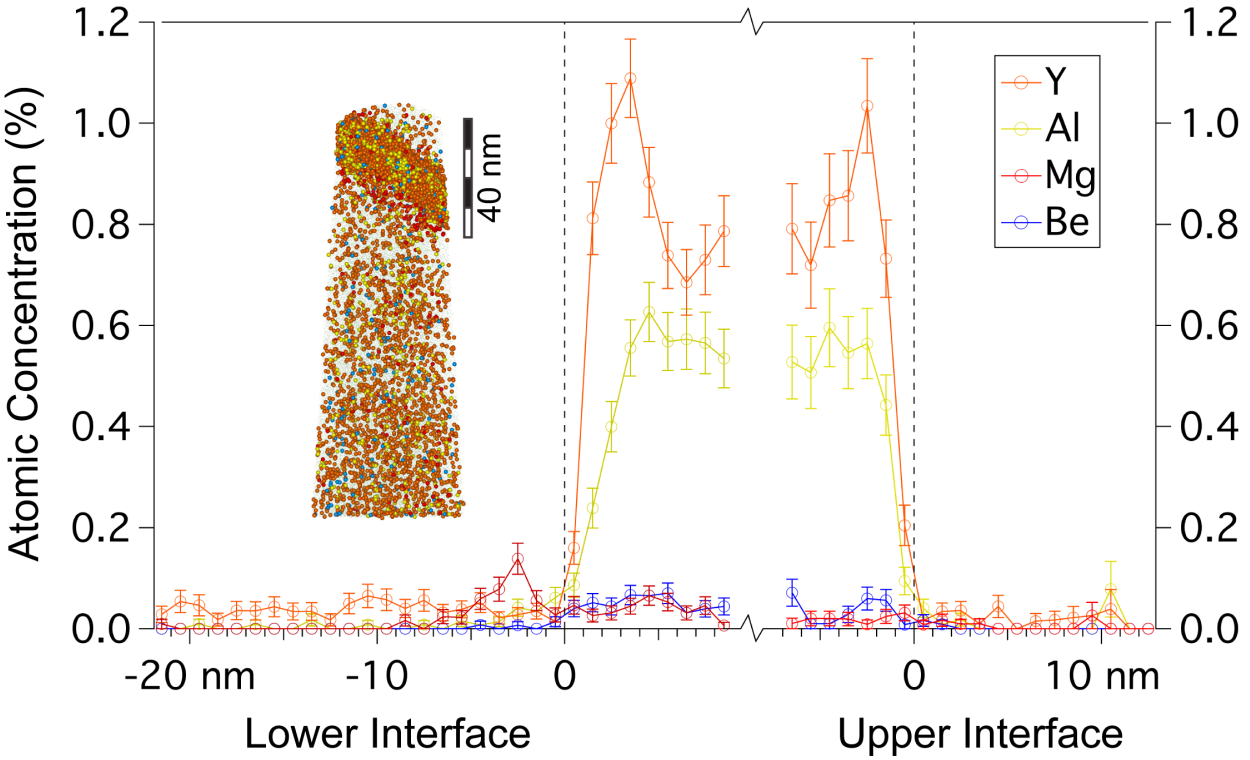

Reddy, S.M., van Riessen, Saxey, D.W., Johnson, T.E., Rickard, W.D.A, Fougerouse, D., Fischer, S., Prosa, T.J., Rice, K.P., Reinhard, D.A., Chen, Y. & Olson, D. 2016. Mechanisms of deformation-induced trace element migration in zircon resolved by atom probe and correlative microscopy. Geochimica et Cosmochimica Acta (2016)

DOI: http://dx.doi.org/10.1016/j.gca.2016.09.019